JGR

Large-scale mantle discontinuity topography beneath Europe: Signature of akimotoite in subducting slabs

Sanne Cottaar[1] and Arwen Deuss[2]

[1]University of Cambridge, Cambridge, UK, [2]Utrecht University, Utrecht, the Netherlands

Abstract The mantle transition zone is delineated by seismic discontinuities around 410 and 660 km, which are generally related to mineral phase transitions. Study of the topography of the discontinuities further constrains which phase transitions play a role and, combined with their Clapeyron slopes, what temperature variations occur. Here we use P to S converted seismic waves or receiver functions to study the topography of the mantle seismic discontinuities beneath Europe and the effect of subducting and ponding slabs beneath southern Europe on these features. We combine roughly 28,000 of the highest quality receiver functions into a common conversion point stack. In the topography of the discontinuity around 660 km, we find broadscale depressions of 30 km beneath central Europe and around the Mediterranean. These depressions do not correlate with any topography on the discontinuity around 410 km. Explaining these strong depressions by purely thermal effects on the dissociation of ringwoodite to bridgmanite and periclase requires unrealistically large temperature reductions. Presence of several wt % water in ringwoodite leads to a deeper phase transition, but complementary observations, such as elevated V_p/V_s ratio, attenuation, and electrical conductivity, are not observed beneath central Europe. Our preferred hypothesis is the dissociation of ringwoodite into akimotoite and periclase in cold downwelling slabs at the bottom of the transition zone. The strongly negative Clapeyron slope predicted for the subsequent transition of akimotoite to bridgmanite explains the depression with a temperature reduction of 200–300 K and provides a mechanism to pond slabs in the first place.

1. Introduction

The Earth's mantle transition zone defines the region between the upper and lower mantle that is characterized by a number of seismic discontinuities. The two strongest discontinuities are global features and lie around depths of 410 and 660 km; they are here referred to as the 410 and 660. These discontinuities are generally associated with two phase transitions with high impedance contrast in the Mg_2SiO_4-system (the "olivine" system). Around 410 km, olivine ($\alpha - Mg_2SiO_4$) converts to wadsleyite ($\beta - Mg_2SiO_4$) in an exothermic reaction [*Katsura and Ito*, 1989]. Around 660 km, ringwoodite ($\gamma - Mg_2SiO_4$) dissociates to periclase and bridgmanite (MgSi-perovskite) in an endothermic reaction [*Ringwood*, 1970; *Ito and Takahashi*, 1989]. The $MgSiO_3$-system (the "nonolivine" or "garnet-pyroxene" system) also predicts phase transitions at the base of the transition zone. At higher temperatures majorite transitions to bridgmanite and at lower temperatures akimotoite (MgSi-ilmenite) transitions to bridgmanite around 660 km [*Yu et al.*, 2011; *Hernández et al.*, 2015]. Observations of splitting of the 660 are attributed to the occurrence of multiple transitions in the $MgSiO_3$- and Mg_2SiO_4-systems [*Simmons and Gurrola*, 2000; *Deuss et al.*, 2006].

The exact depth at which each phase transition occurs, depends on temperature, composition [*Xu et al.*, 2008; *Cammarano et al.*, 2005; *Cobden et al.*, 2008; *Cammarano et al.*, 2009], and water content [*Litasov et al.*, 2005b; *Ghosh et al.*, 2013]. The behavior of each phase transition is generally defined by its Clapeyron slope. Seismic mapping of the topography on the discontinuities related to these transitions gives insight to lateral variations of temperature (and potentially composition) in the deep mantle. Where the mantle is cold, the olivine-wadsleyite transition around 410 km (which has a positive Clapeyron slope) occurs shallower, and where the mantle is hot, it occurs deeper. The dissociation of ringwoodite around 660 km has an opposite signature (i.e., a negative Clapeyron slope), occurring deeper at cold temperatures and shallower at hot temperatures. The mantle transition zone bounded by these two transitions therefore thickens in cold regions and thins in hot regions. Compositional variations in terms of the amount of basalt have minimal effects on the transition depths, especially when it is mixed in and not equilibrated [*Xu et al.*, 2008].

Besides temperature, water content is thought to play a role in the transition zone. Wadsleyite and ringwoodite have strong water solubility [overview in *Ohtani*, 2015]. The hypothesis that water is stored in the transition zone has become more probable with the recent observation of hydrous ringwoodite in an ultra-deep diamond [*Pearson et al.*, 2014]. Water content has a significant effect on the phase transitions. Similar to cold temperatures, increased water content thickens the transition zone by shallowing the olivine-wadsleyite transition around 410 km [*Frost and Dolejš*, 2007] and deepening the dissociation of ringwoodite, while also increasing its sensitivity to temperature [*Litasov et al.*, 2005b; *Ghosh et al.*, 2013].

Studying these phase transitions is also important as they influence global mantle dynamics. The thermodynamics of transitions with a negative Clapeyron slope and the increase in viscosity around 660 km have an inhibiting effect on convection [*Christensen and Yuen*, 1985; *King et al.*, 2015]. In tomographic models, subducting slabs are seen ponding above and below the 660 in several locations across the globe [*Fukao and Obayashi*, 2013]. Local tomographic models beneath Europe also indicate accumulation of fast material at the bottom of the mantle transition zone resulting from subduction of the Tethys ocean [*Wortel and Spakman*, 2000; *Faccenna et al.*, 2003; *Zhu et al.*, 2012, 2015]. The purpose of our study is to map the effects of the subducting slab material around the Mediterranean on the seismic discontinuities.

As data coverage across Europe has increased in the past decade, we conduct a continent-wide study of *P*-to-*s* conversions or receiver functions. We map the mantle transition zone beneath northern Europe as stable reference region in contrast to the perturbations we expect beneath southern Europe from the subducting slabs. The *P*-to-*s* conversions are studied through iterative deconvolution leading to so-called receiver functions (section 2.1), which, after quality control (section 2.2), are stacked in a common conversion point (CCP) stack (section 2.4). We apply the most recent adjoint tomography models for *P* and *S* wave velocity [*Zhu et al.*, 2015] to correct for velocity variations above the discontinuities (section 2.3). This allows us to present the results in terms of the absolute depths of the discontinuities instead of the relative thickness of the mantle transition zone (section 3). We discuss the robustness of the results and its implications in terms of temperature, water content, and the role of $MgSiO_3$ phases (section 4).

2. Methods

2.1. *P*-to-*s* Receiver Functions

When compressional waves (*P*) interact with a velocity discontinuity part of their energy converts to shear waves (*S*). Converted shear phases from the mantle transition zone arrive 40 to 70 s after the direct *P* arrival on the radial component of a seismogram and are hereafter named P410s and P660s. We use the delayed timing of this converted energy to map out the depth at which the conversion occurs [*Vinnik*, 1977; *Langston*, 1977]. *P*-to-*S* conversions have been used to study the mantle transition zone on a global scale [*Lawrence and Shearer*, 2006; *Andrews and Deuss*, 2008], in continental settings [e.g., *Lebedev et al.*, 2003; *Schmandt et al.*, 2012; *Tauzin et al.*, 2013], and on a regional scale [e.g., *Emry et al.*, 2015; *Thompson et al.*, 2015].

To make the converted *P*-to-*s* phases visible, we need to deconvolve the source component from the traces. We assume that the main *P* arrival on the vertical component is a representation of the source, and thus, we deconvolve the vertical component from the radial component resulting in a time series named a receiver function. Before deconvolution, the data are filtered with a low pass filter of 0.2 Hz and a window is cut from 25 s before to 150 s after the main *P* arrival. There are a number of time and frequency-domain methods to perform the deconvolution, but the differences in results are minimal (Spieker, Rondenay, and Halpaap, manuscript in preparation, 2015). Here we deconvolve using the iterative deconvolution in the time domain [*Ligorria and Ammon*, 1999]. The receiver function is constructed by iteratively adding Gaussian pulses to the time series. The timing and amplitude of each pulse is determined by the following steps: the current (initially empty) receiver function is convolved with the vertical component; the convolved time series is subtracted from the radial component to give the misfit; the misfit time series is cross correlated with the vertical component; and the maximum of this cross-correlated function indicates the time and amplitude for a new Gaussian peak in the receiver function. The iteration stops when adding more pulses has insignificant effect on the overall fit or when 200 Gaussian pulses have been added, assuming noise is being fitted at that stage. The Gaussian pulses used to construct the receiver function time series have a width of 5 s.

2.2. Data Selection

Data are collected from the Observatories and Research Facilities for European Seismology (ORFEUS) and Incorporated Research Institutions for Seismology (IRIS) databases for earthquakes with magnitudes (Mw)
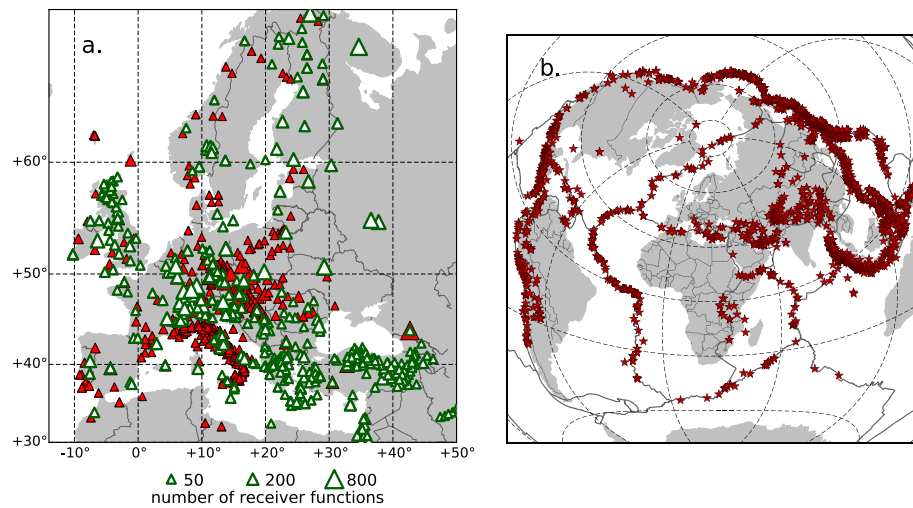
Figure 1. (a) Map showing the distribution of stations across Europe used in this study. The station triangles are scaled to the number of high quality receiver functions. Triangles represent the ~45,000 receiver functions used in Figures 2 and 3a. Green/white triangles indicate stations used in the final common conversion point stack (~28,000 receiver functions). (b) Map showing locations of 2345 earthquakes used at a distance from 30 to 90° from European stations (stars).

larger than 5.5 and at epicentral distances of 30 to 90° for stations across Europe which were active within the period of 2000 to 2014. This results in ~490,000 events to station pairs. We download, process, and filter the data using ObsPy [*Beyreuther et al.*, 2010]. We initially automatically assess the quality of the data by comparing the mean energy of the direct *P* wave arrival (in a 25 s window) to the mean energy on the radial component (in 190 s window). The data are included when this signal-to-noise ratio exceeds 2, a value benchmarked by manually assessing a subset of the data. Data from Iceland are excluded, as this region is studied in more detail by *Jenkins et al.* [2016]. Mostly data from earthquakes with a relative small magnitude at a large epicentral distance fail this test. We retain ~150,000 event-station pairs.

After creating the receiver functions, we include several more quality checks. First, recorrelating the receiver function with the vertical component needs to resolve at least 60% of the radial component. Second, the main *P* wave arrival needs to be within 1 s from zero, i.e., the waveforms on the vertical and radial component
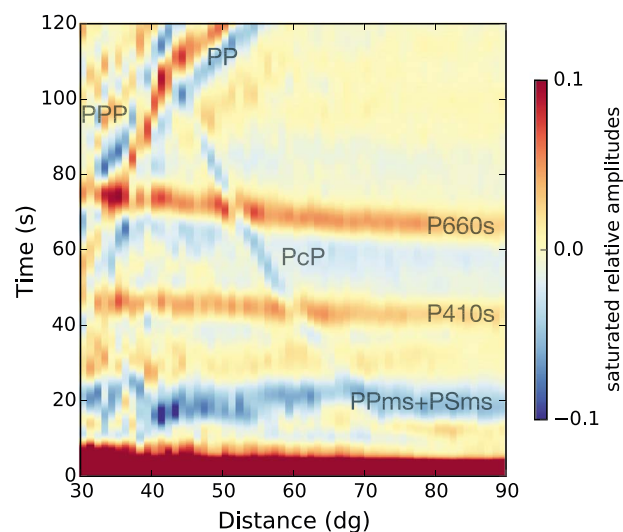

Figure 2. Stack of high quality receiver functions (~45,000), renormalized in distance bins of one degree as a function of time aligned on the main *P* arrival. Arrivals are indicated for the P410s, P660s, PcP, PP, PPP, and crustal reverberations (PPms + PSms).
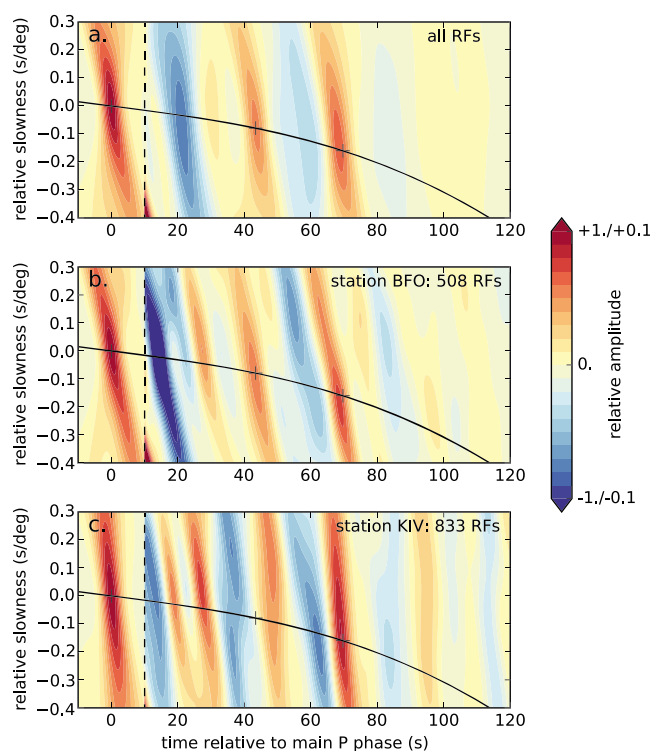
Figure 3. Slowness stacks for (a) ~45,000 high quality receiver functions, (b) 508 receiver functions at station BFO (network II), and (c) 833 receiver functions at station KIV (network II). Time and slowness are with respect to the direct *P* arrival. Slowness predictions for *P*-to-*s* conversions in PREM lie along the black line. The direct P, P400s, and P670s are indicated by black crosses at 0, 44, and 70 s, respectively. The entire stack is normalized to the direct *P* wave arrival, while the amplitudes past 10 s are saturated at 0.1.

should correlate well. Lastly, we exclude receiver functions which contain arrivals with amplitudes stronger than 40% of the main *P* arrival, either before or after the *P* wave arrival. After these tests, we have ~45,000 receiver functions left in our data set (Figure 1).

The converted phases are rarely visible in an individual receiver function and many need to be combined in a stack to analyze the arrivals. Figure 2 shows a moveout stack, where all ~45,000 receiver functions are stacked in 1° epicentral distance bins. The P410s and P660s are clear positive arrivals with a slight negative moveout relative to the main *P* phase. The PcP and PP(P) phases interfere at specific distance ranges, but as they have very different moveout from the converted phases, they will not stack coherently in our further stacking techniques.

In Figure 3a all high quality receiver functions are stacked in a slowness stack or vespagram, i.e., a time versus slowness plot. This method assumes a constant differential slowness for the converted phases with epicentral distance. For each horizontal slowness, all the receiver functions are stacked after shifting them to a reference epicentral distance of 65° using the assumed slowness. The P410s and P660s arrivals stack coherently at a slight negative slowness. P660s arrives slightly earlier than the predicted time for P670s for preliminary reference Earth model (PREM) [*Dziewonski and Anderson*, 1981]. The crustal reverberations are visible around 24 s, but the PcP and PP(P) observed in Figure 2 lie outside the slowness range shown here. We also compute local or single station slowness stacks to check for any local complexities. Figures 3b and 3c show examples of single station stacks which contain additional arrivals at a slightly positive relative slowness. These arrivals are reverberations or multiples, i.e., phases that have reflected at the surface and then reflected and converted on shallower discontinuities. The timing and slowness of the multiples varies strongly across localized stacks. Figure 3b is a slowness stack for station beat frequency oscillator (BFO) in Switzerland with a strong multiple around 58 s, but the converted phases from 410 and 660 are still identifiable, so we will keep this station in our data set. Figure 3c is an example from station KIV in Russia with a high number of high quality receiver functions but shows unfortunate strong interference of multiples around the expected arrival time of P410s.
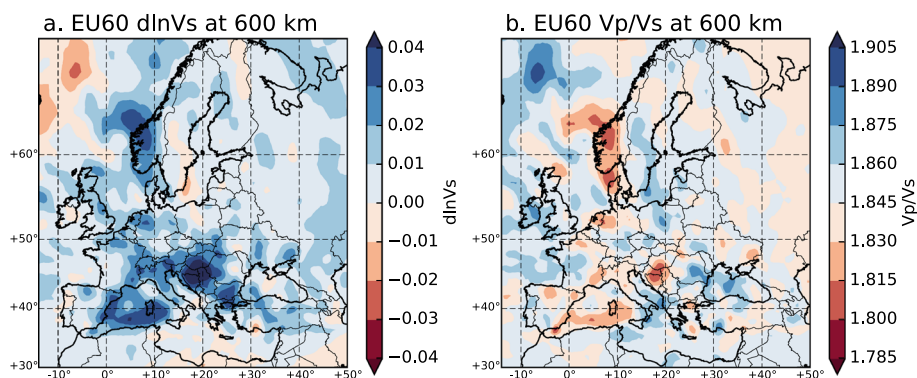
Figure 4. (a) Shear wave velocity variations and V_P/V_S ratio at 600 km depth in EU60 [*Zhu et al.*, 2015].

This is an example of a station that we exclude for our analysis of the 410. If there are sufficient data at a station, we also compute slowness stacks for azimuth and distance bins and often see that the multiples come from a specific direction that need to be excluded. Our final data set contains, respectively, ~26,800 and ~28,000 receiver functions for common conversion point stack of the 410 and 660.

2.3. Time-Depth Conversions

We use two different velocity models to convert the receiver functions from time to depth; the 1-D radial model, PREM [*Dziewonski and Anderson*, 1981], and the 3-D velocity model, EU60 [*Zhu et al.*, 2015]. EU60 is an adjoint tomographic model of the crust and upper mantle beneath Europe for both S and P wave velocities (as well as attenuation and anisotropy, which are not used here). The initial crustal model is EPcrust [*Molinari and Morelli*, 2011] which describes the crust every 0.5° in terms of a sediment, upper crustal, and lower crustal layer. The crustal model is modified in the 60 iterations resulting in EU60. We use the modified crustal model in EU60 for our corrections, except for some locations where we remove unrealistic low velocities (down to 1 km/s) from the very top layer. Because of the inclusion of body waves, the EU60 model has good ray coverage down to the mantle transition zone. The shear wave velocity variations and V_P/V_S ratios in EU60 at 600 km depth in the mantle transition zone are shown in Figure 4.

For 1-D PREM we use TauP [*Crotwell et al.*, 1999] to calculate the travel time predictions for the converted phases using the epicentral distance and event depth for each receiver function. For the 3-D models, we ray-trace the P and S phase backward through the model along the great circle path. The 3-D velocity corrections above the 410 are of the order of several seconds, with a maximum value of 4 s, translating to corrections of up to ~20 km for the discontinuity topography. Within the transition zone most of the corrections are less than 0.5 s with maximum values of −1.3 s beneath the Balkan, which translates to a deepening of the 660 of about 8 km.

2.4. Common Conversion Point Stacking

While receiver functions carry their name because early arrivals are assumed to represent the crustal structure directly beneath the receiver, this assumption does not hold for converted phases from the mantle transition zone. Receiver functions at one station can contain conversions from earthquakes with different back azimuths that sample a region in the mantle transition zone with a radius of 500 km. To take this into account, we use common conversion point (CCP) stacking [e.g., *Dueker and Sheehan*, 1997]. The stack is built on a grid beneath Europe with a grid spacing of 0.5° in latitude and longitude and 2 km in depth between 60 and 1200 km. We use the back-propagated ray to stack the receiver function energy into the nearby grid points weighted by a factor. The weighting factor follows *Lekic et al.* [2011] and is based on the fresnel zone half width, Δ^{HW}, for a wavelength, λ, at the specific depth, z, defined as:

$$\Delta^{HW} = \sqrt{\left(\frac{\lambda}{3} + z\right)^2 - z^2}. \tag{1}$$
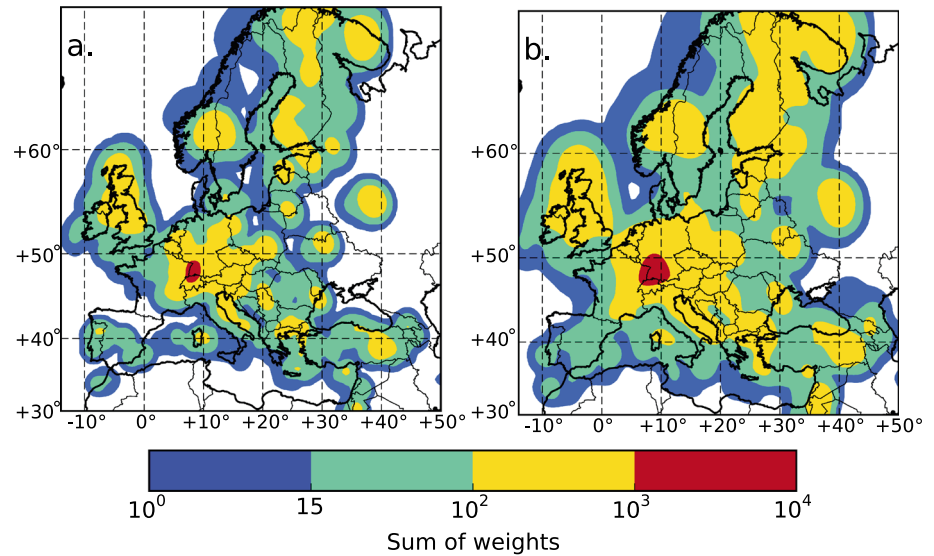
Figure 5. Sum of the weights in the common conversion point stacks at (a) 410 and (b) 660 km depth.

Here we use the wavelength for a 10 s shear wave. The weights are a normalized cubic spline based on the distance of a grid point to the ray path normalized by the fresnel zone half width, $\bar{\Delta} = \Delta/\Delta^{HW}$:

$$w = \begin{cases} \frac{3}{4}\bar{\Delta}^3 - \frac{3}{2}\bar{\Delta}^2 + 1 & \text{if } \bar{\Delta} \leq 1 \\ \frac{1}{4}(2 - \bar{\Delta})^3 & \text{if } 1 < \bar{\Delta} \leq 2 \\ 0, & \text{if } \bar{\Delta} \geq 2. \end{cases} \tag{2}$$

This formulation allows for some smoothing over an area of twice the fresnel zone width, although weights outside the fresnel zone are less than $\frac{1}{4}$. Finally, each grid point is divided by the sum of the total weights. In addition to calculating the weighted average, we also track a running standard error at each grid point, i.e., the standard error at each grid point is updated with each new data point using the weighted average of the data so far. Figure 5 shows the data coverage in terms of the sum of the total weight through slices in the stack at 410 and 660 km. The coverage is wider for 660 km depth because the distribution of ray piercing points and the fresnel zone, from which the weights are computed, widen with depth. The coverage is densest just north of Switzerland because of the large number of arrivals from events in Asia at the station network CH of the Swiss Seismological Network and stations BFO and GRFO of the Global Seismographic Network. We mask regions with a weighted sum less than 15.

3. Results

We use our receiver function data set to make common conversion point (CCP) stacks for the 410 and 660. Maps of the resulting topography on the 410 and 660 (Figure 6) are constructed by picking the depths at peak amplitudes between 370 and 450 km depth for the 410 and between 620 and 700 km depth for the 660. Figures 6a and 6b show the topography of the discontinuities using 1-D PREM to convert from time to depth. The median values of the 410 and 660 lie at 404 and 656 km. When using the 1-D velocity model, the broadscale topography shows strong correlations between the 410 and 660 topography; beneath northern Europe, and especially beneath the cratons in the northeast, both discontinuities appear shallow, while both discontinuities appear deep beneath southern Europe (Figures 6a and 6b). These correlations reflect the lack of corrections for 3-D upper mantle velocity variations. On top of these broadscaled features, there is small-scale scatter visible in the topography, mainly on the 410 and dominantly around the Mediterranean. While care is taken to exclude data which contain strong multiples interfering with the converted phases from the 410 to 660 (section 2.2), we can only identify problematic mulitples if they interfere with converted arrivals in slowness stacks for individual stations or groups of stations. In some individual stacks, multiples come from a specific direction or within a specific distance range, but sufficient data from other angles result in high quality P410s and P660s in the slowness stack. These multiples can still cause local artifacts in the CCP stack. Although strong topography over short length-scales has been observed before
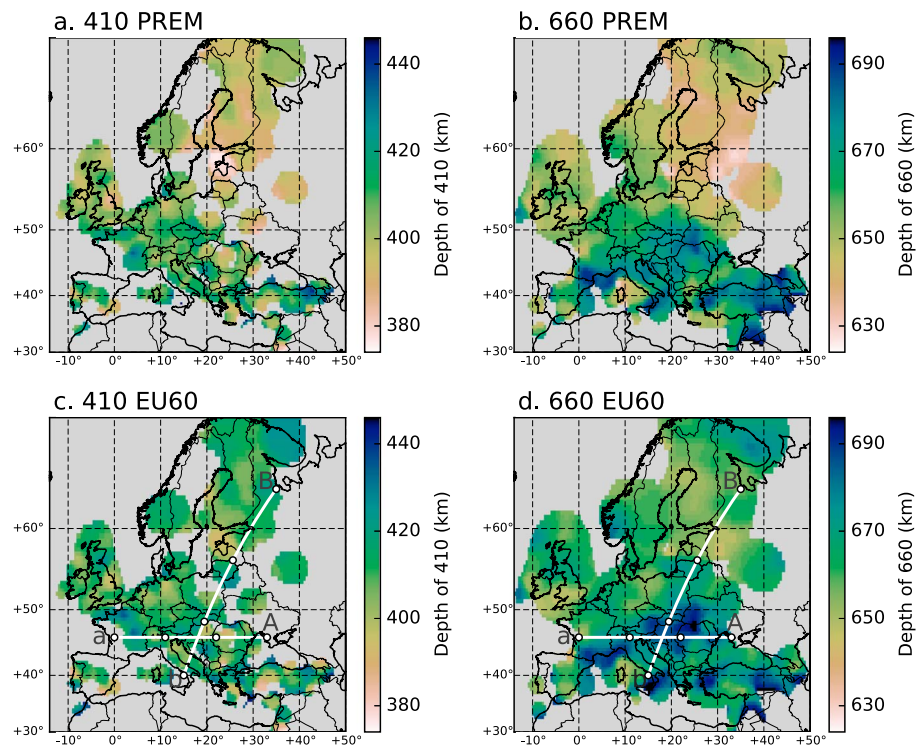
Figure 6. Topography on (a) the 410 and (b) the 660 converted from time to depth using 1-D model PREM and topography on (c) the 410 and (d) the 660 converted to depth using 3-D model EU60. a-A and b-B indicate the cross sections shown in Figure 7.

[*Day and Deuss*, 2013], we will focus our interpretation on the broadscale features that are robust across many stations and assume the small-scale scatter on the 410 topography is an artifact from multiples resulting from shallow structural complexities around the Mediterranean.

Figures 6c and 6d show the topography on the discontinuities corrected using 3-D velocity variations from the EU60 model. The correlation between the topography of the 410 and 660 is now largely removed and also the variance of the topography on both discontinuities is strongly reduced. Median values lie at 412 and 666 km for the 410 and 660, respectively. The 410 shows little broad scale topographic variations and, in regions without scatter, lies at ~410 km. This observation gives confidence to our crustal and upper mantle corrections. The 660 topography on the other hand mainly lies between 650 and 690 km, with broad depressions down to 690 km occurring beneath central Europe, the southern tip of Italy and around Turkey. The 660 beneath northern Europe lies around 660 km depth and has relatively little topography.

Several smaller-scaled studies using teleseismic receiver functions across Europe confirm our topography observations. Studies beneath Germany [*Knapmeyer-Endrun et al.*, 2013] and Finland [*Alinaghi et al.*, 2003] find an average and uniform transition zone as we see in the same regions beneath northern Europe. Studies beneath eastern Turkey [*Ozacar et al.*, 2008], the Alps [*Lombardi et al.*, 2009], and the Mediterranean [*van der Meijde et al.*, 2005], observe a deep 660 or thickened mantle transition zone in agreement with our observations beneath central and southern Europe. A deep 660 is also found using IberArray (not included here) beneath Iberia and Gibraltar [*Bonatto et al.*, 2013; *Morais et al.*, 2015]; we roughly confirm these results, but our coverage is limited in this region.

Cross sections through the CCP stack for the regions with strong depressions of the 660 are shown in Figure 7. Cross section a-A runs beneath central Europe and shows that the 660 deepens from west to east. The depression on the 660 correlates with widespread fast anomalies in the mantle transition zone seen in tomographic model EU60. Cross section b-B runs from central Europe to the Eastern European craton. This cross section shows the contrast of the deep 660 beneath central Europe and the shallower 660 beneath the craton in the northeast, where the tomographic velocities in the transition zone are also slower. In the boundary region between these two areas (around 14 to 17° along the cross section) the amplitudes of the 660 are reduced,
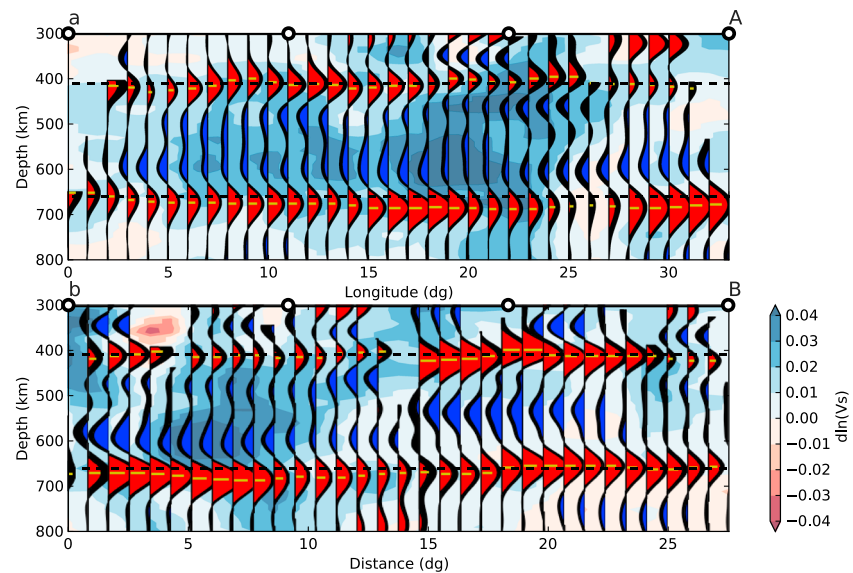
Figure 7. Cross sections through the CCP stack with 3-D velocity corrections from west to east across central Europe (a-A) and from central Europe across the Eastern European craton (b-B) as indicated in Figures 6c and 6d. Profiles from the CCP stack are shown as a conventional receiver function where significant positive arrivals are in red and significant negative arrivals in blue. Significant arrivals are those with amplitudes above twice the standard error, and the depths of the maximum amplitudes for P410s and P660s are indicated by yellow bars. Parts of the stack with insufficient coverage are masked. The background is the shear wave velocity from model EU60 saturated at $+/-4\%$. Black dashed lines show reference depths at 410 and 660 km.

which is likely related to less coherent stacking due to the strong topography on the 660. In both cross sections the amplitudes of the depressed 660 are strong and the standard errors are low. The 410 across both sections shows smaller-scale scatter on its topography and regions with reduced amplitudes. Within the transition zone, there are also widespread negative arrivals, although separate analysis of their slownesses indicates that some of these arrivals are multiples from shallower structure, and detailed analysis of these arrivals is beyond the scope of this study.

We finally take depth profiles from every horizontal grid point in the CCP stack with a significant P410s and P660s arrival and stack these in bins of their respective depth of the 660 ranging from 646 to 690 km (following *Tauzin and Ricard* [2014]). The 410 amplitude is generally reduced due to incoherent stacking, and the trend of its peak shows no (anti-) correlated topography compared with the 660 (Figure 8). This exercise confirms that the strong depressed topography on the 660, which we observe in our study, is indeed unrelated to topography on the 410.

4. Discussion

Across Europe we observe stronger topography on the 660 than on the 410. The topography on the 660 ranges across 40 km, but shows localized depressions of up to ∼30 km in depth relative to 660 km, in regions beneath central Europe and around the Mediterranean, with no correlating anomalous topography found on the 410. Here we first discuss the robustness of the observed topography and then the likelihood of three alternative interpretations of the observed depression on the 660, i.e., due to purely thermal variations, the presence of water, or the dominance of akimotoite within subducting slabs.

4.1. Robustness of Observed 410 and 660 Topography
The observed topography depends on the quality of the corrections for 3-D velocity variations above the discontinuities. Concerns might arise that velocity anomalies in the deep mantle are underestimated due to wavefront healing effects [*Nolet and Dahlen*, 2000], but the full-waveform adjoint tomographic methodology used by *Zhu et al.* [2015] is less sensitive to these effects. *Zhu et al.* [2015] also account for transition zone topography, but their topography—for the 660 it gradually varies from 630 km in the southwest to 660 km in the northeast of Europe—is very different from the observed topography here. Incorrect discontinuity topography in a tomographic model could leak into velocity anomalies around the 410 and 660.
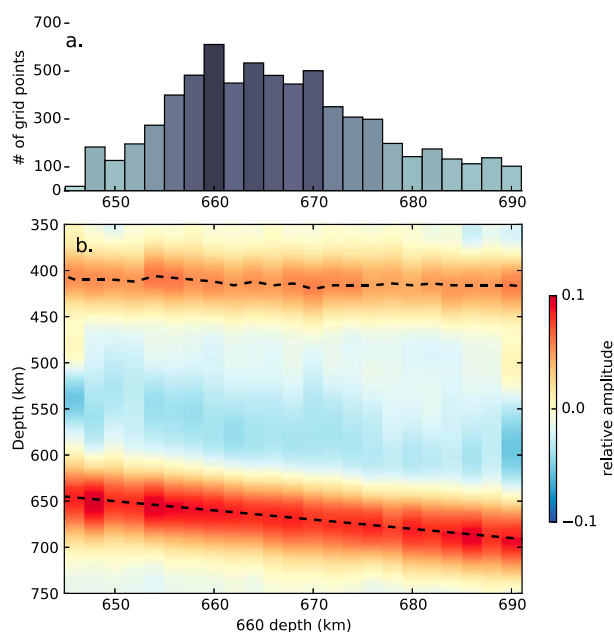
Figure 8. Stack of vertical profiles from each grid point in the CCP stack for 2 km bins based on the depth of the 660 ranging from 646 to 690 km. (a) Histogram of the number of profiles in each bin. (b) Amplitudes as a function of depth in the stacked bins.

What if the observed topographic signature were due to unmodeled velocity variations in the true Earth? Let's apply the thought experiment that the variations seen on the 660 (and not seen on the 410) are due to unseen velocity anomalies within the mantle transition zone. To remove the strong depressions seen on the 660, the velocities across the transition zone would have to be on the order of 10% slower than PREM. We find instead that the depressions correlate with regions of fast shear velocity anomalies in the transition zone in the EU60 model of *Zhu et al.* [2015] (Figures 4–7). Correcting for these fast anomalies actually increases the depressions further with a maximum correction of 8 km. To argue that the depressions are due to unmodeled velocity variations in the mantle transition zone would imply that tomographic model EU60 has the wrong sign for the velocity anomalies, which seems very unlikely. If the fast anomalies in the mantle transition zone in the EU60 model were underestimated, this would mean the true depressions on the 660 are even deeper.

In a second thought experiment, we attribute the depressed 660 to incorrect velocity corrections above the 410, where any unmodeled velocity anomaly affects the topography on both transition zone discontinuities. Including a slow velocity anomaly in the model used for the velocity corrections would map both discontinuities shallower. In the anomalous regions, this would create an upwarp on the 410, which is otherwise at average depth, and decrease the depression on the 660, causing an overall anticorrelation between the topography of the two discontinuities that could be attributed to cold temperatures in a olivine-rich mantle. The regions of the anomalous depressed 660 do not correlate directly with slow velocity anomalies in the shallower mantle in the EU60 model that could be underestimated in the inversion process. Additionally, the depressions beneath central Europe are in locations with strong data coverage both in the tomographic model [*Zhu et al.*, 2015] and in this study (Figure 6), and it is hard to imagine that slow seismic anomalies would not be properly imaged in these regions. Thus, we conclude that the deepening of the 660 is a robust feature in our data that needs to be explained by a process only affecting the 660.

4.2. Purely Thermal Signature?

The broadscale topography observed on the 410 of less than 20 km leads to estimates of temperature variations ranging from 180 K, using a Clapeyron slope of +4 MPa/K [*Katsura et al.*, 2004], to 340 K, using a slope of +2.5 MPa/K [*Katsura and Ito*, 1989]. Because the 410 and 660 have Clapeyron slopes of opposite signs in the olivine system, any temperature anomaly across the mantle transition zone is expected to lead to anticorrelated anomalies on these discontinuities. The deep, depressed anomalies in the 660 topography of down to 690 km depth seen here do not correlate with elevations on the 410 in the same regions (Figure 8), so they must be due to effects local to the 660. Let us first investigate the local temperature anomalies required
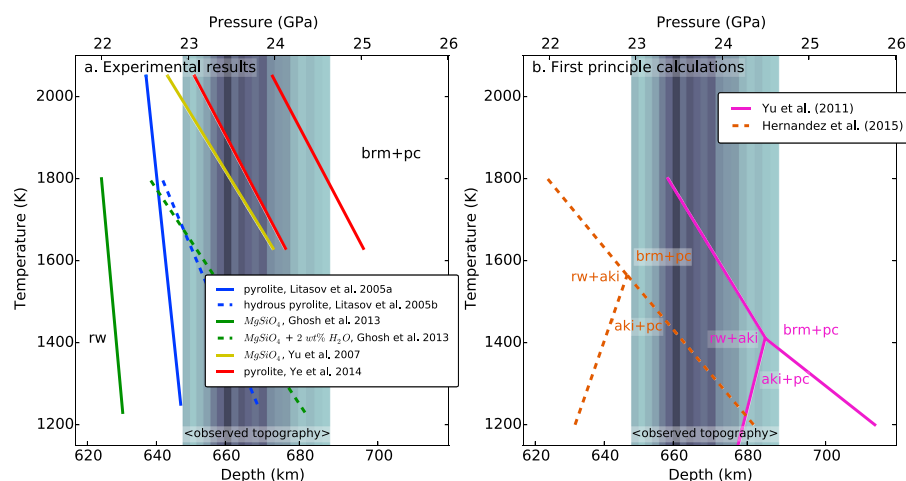
Figure 9. Range of 660 topography observed across Europe in this study compared to Clapeyron slopes for various phase transitions. Observed seismic topography is shown in grey shaded bins based on the histogram in Figure 8a. (a) Clapeyron slopes from experiments for the dissociations of ringwoodite to bridgmanite and periclase are shown for dry (solid blue) [*Litasov et al.*, 2005a] and hydrous (dashed blue) [*Litasov et al.*, 2005b] pyrolite in a multianvil press; dry (solid green) and hydrous (dashed green) ringwoodite in a multianvil press [*Ghosh et al.*, 2013]; and dry pyrolite in a diamond anvil cell (red) [*Ye et al.*, 2014]. Also shown are the results from the first principle calculations of *Yu et al.* [2007] (yellow). (b) First principle calculation results for the stability field of akimotoite and periclase at relatively low temperatures [*Yu et al.*, 2011; *Hernández et al.*, 2015]. *Hernández et al.* [2015] present variations in the Clapeyron slope in pressure and temperature, but these are here shown by their mean constant Clapeyron slope. aki = akimotoite, rw = ringwoodite, pc = periclase, and brm = bridgmanite.

to explain the depressions by the stagnation of cold subducting slab material on top of the 660. Using a Clapeyron slope of −2.5 MPa/K [*Ye et al.*, 2014] for the dissociation of ringwoodite to bridgmanite in a pyrolitic sample requires temperature variations of ~680 K to explain the maximum topography of 40 km seen across Europe (Figure 9a). Older experimental estimates of smaller Clapeyron slopes on the order of −0.5 MPa/K [e.g., *Litasov et al.*, 2005a] would lead to even higher and more unrealistic estimates. Clapeyron slopes proposed by first principle calculations of −2.9 MPa/K [*Yu et al.*, 2007] and −3.9 MPa/K [*Hernández et al.*, 2015] are on the higher end, and reduce the predicted anomaly to 400–600 K. Whether these values are realistic depends on how cold ponding slabs interact with the 660 [*Garel et al.*, 2014; *King et al.*, 2015]. While these predicted values are much larger than those for the topography on the 410, we exclude purely thermal effects as the cause for the strong topography observed on the 660.

4.3. Signature of Increased Water Content?

Previous studies have interpreted observations of depressed 660 in terms of increased water content in regions where subducted slabs are seen by increased shear wave velocities within the transition zone. Such strong depressions on the 660 in regions with subducting slabs have been seen beneath the Philippines [*Suetsugu et al.*, 2010], the western United States [*Cao and Levander*, 2010], the Red Sea [*Mohamed et al.*, 2014], and Korea [*Lee et al.*, 2014]. Experiments on ringwoodite and pyrolite samples hydrated with 2 wt % water show an increased pressure of the dissociation of ringwoodite and a steeper Clapeyron slope [*Litasov et al.*, 2005b; *Ghosh et al.*, 2013, Figure 9a]. Thus, the deep topography on the 660 could be attributed to a combination of lower temperatures and the presence of several wt % water in the subducted slab material.

However, complementary geophysical observables predicted for hydrous ringwoodite are not seen beneath central Europe. Including 1 wt % water in ringwoodite lowers V_S by −2.5% while having little effect on V_P [*Jacobsen and Smyth*, 2006], increasing the V_P/V_S ratio by several percent. The reduction in shear velocities and increase in V_P/V_S ratio for 1–2 wt % water content are so strong that it would take extremely reduced temperatures to compensate and lead to an overall increase in velocity, i.e., a 1 wt % increase in water content causes a velocity reduction equivalent to 200–350 K temperature increase [*Jacobsen and Smyth*, 2006; *Panero*, 2010]. We found that the depressions correlate with an increase instead of reduction in shear wave velocity in EU60 (Figures 4–7). In addition, the P wave velocities in EU60 in the same regions are increased to a lesser extent, reducing the V_P/V_S ratio. Increased water content also leads to an increase in attenuation [*van der Lee and Wiens*, 2006]. However, while *Zhu et al.* [2013, 2015] find elevated attenuation at the top of downgoing
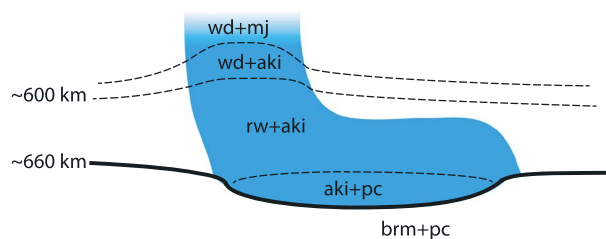
Figure 10. Cartoon of the interpretation of ringwoodite dissociating within the slab and the subsequent deep transition of akimotoite to bridgmanite (the vertical axis is exaggerated). wd = wadsleyite, mj = majorite, aki = akimotoite, rw = ringwoodite, pc = periclase, and brm = bridgmanite.

slabs, there is no correlation between attenuation at the base of the transition zone and the depressions at 660 observed here. Lastly, studies of electrical conductivity in the transition zone beneath central Europe do not see the expected elevated conductivity for a wet transition zone [*Tarits et al.*, 2004; *Utada et al.*, 2009]. The lack of these complementary observables makes the hypothesis that the depressions on the 660 seen here relate to widespread ponding of hydrous ringwoodite unlikely.

4.4. Signature of Akimotoite in Subducting Slabs

Another hypothesis for the presence of strong depressions at ponding slabs is the dominance of akimotoite at lower temperatures as proposed by *Yu et al.* [2011] based on first principle calculations. Their calculations show that ringwoodite dissociates to akimotoite and periclase at the bottom of the transition zone and temperatures beneath 1400 K (Figures 9b and 10). Thus, akimotoite might be the most abundant phase in the center of cold subducted slabs at the base of the mantle transition zone. The Clapeyron slope of the akimotoite-to-bridgmanite transition is predicted to be relatively large, varying from −2.7 MPa/K [*Hirose et al.*, 2001] to −4 MPa/K [*Chudinovskikh and Boehler*, 2004] in experimental studies, and calculated to be −4 MPa/K [*Hernández et al.*, 2015], −5 MPa/K [*Wentzcovitch et al.*, 2004], and −6 MPa/K [*Yu et al.*, 2011] in first principle studies. The high-end values of −5 − −6 MPa/K are able to explain the 30 km localized depressions we observe in the 660 topography by moderate temperature reductions of ∼200 – 300 K. The presence of akimotoite is consistent with cold temperatures and thus with the observation of fast shear velocities within the transition zone, but it would only require a moderate temperature anomaly.

If the seismic discontinuity at ∼660 km beneath subducted slabs is indeed dominated by the akimotoite transition with a strong negative Clapeyron slope, then this simplifies the mechanism causing slabs to pond in the transition zone. Most of the predicted Clapeyron slopes for this phase transition are past the critical value of −4 MPa/K needed to generate sufficient negative buoyancy for a slab to stagnate [e.g., *Christensen and Yuen*, 1985; *King et al.*, 2015].

The presence of various phase transitions around 660 km depth, each dominant at different temperatures provides additional constraints on using 660 topography as a thermometer for absolute temperatures. Combining the results of *Yu et al.* [2011] with the topography seen here suggests that the temperature in the regions with the strong depressions in 60 topography varies between 1350 and 1500 K. However, there is still uncertainty in the pressure and temperature of the triple point of (rw + aki)–(aki + pc)–(brm + pc) that might affect this interpretation (Figure 9b) [e.g., see *Hernández et al.*, 2015]. In this scenario, we also expect the occurrence of multiple phase transitions and corresponding multiple seismic discontinuities in the slab (Figure 9). However, the predicted shear wave velocity constrast for the dissociation of ringwoodite to akimotoite is several times weaker than that for the transition from akimotoite to bridgmanite [computed using BurnMan *Cottaar et al.*, 2014 and the mineral database of *Stixrude and Lithgow-Bertelloni*, 2011]. Combined with the predicted proximity of the two transitions, it might be difficult to detect this double transition using receiver functions.

5. Conclusions

We combine around 28,000 *P*-to-*s* receiver functions in a common conversion point stack beneath Europe. To analyze the absolute depth of the mantle transition zone discontinuities we apply corrections for shallow velocity variations using the results from the recent adjoint tomographic model EU60 [*Zhu et al.*, 2015]. These corrections strongly reduce the correlations of topography on the 410 and 660. We find that the

410 lies around 410 km depth with long wavelength topography of less than 20 km. The 660 on the other hand shows localized long-wavelength depressions down to 690 km beneath central Europe and around the Mediterranean. These depressions correlate with fast velocities in the transition zone in the EU60 model, so we interpret the occurrence of the depression to be linked to the subduction and ponding of slabs in the transition zone. Explaining the depression by purely thermal effects of the dissociation of ringwoodite requires unrealistic strong reduction in temperature. Alternatively, the presence of water would produce the correct signature on the 660 topography. However, other geophysical observables associated with high water content, such as low V_S, high V_P/V_S ratio, high attenuation and high electrical conductivity, are not observed beneath central Europe. Our preferred hypothesis is the dissociation of ringwoodite into akimotoite and periclase which appears at temperatures beneath 1400 K [*Yu et al.*, 2011] and is likely to occur within subducting slabs. The subsequent phase transition from akimotoite to bridgmanite has a strong negative Clapeyron slope which can both explain the presence of a deep 660 as well as the existence of slab ponding in the transition zone.

References

Alinaghi, A., G. Bock, R. Kind, W. Hanka, and K. Wylegalla (2003), Receiver function analysis of the crust and upper mantle from the North German Basin to the Archaean Baltic Shield, *Geophys. J. Int.*, 155(2), 641–652, doi:10.1046/j.1365-246X.2003.02075.x.

Andrews, J., and A. Deuss (2008), Detailed nature of the 660 km region of the mantle from global receiver function data, *J. Geophys. Res.*, 113, B06304, doi:10.1029/2007JB005111.

Beyreuther, M., R. Barsch, L. Krischer, T. Megies, Y. Behr, and J. Wassermann (2010), ObsPy: A Python toolbox for seismology, *Seismol. Res. Lett.*, 81(3), 530–533, doi:10.1785/gssrl.81.3.530.

Bonatto, L., M. Schimmel, J. Gallart, and J. Morales (2013), Studying the 410-km and 660-km discontinuities beneath Spain and Morocco through detection of *P*-to-*s* conversions, *Geophys. J. Int.*, 194(2), 920–935, doi:10.1093/gji/ggt129.

Cammarano, F., S. Goes, A. Deuss, and D. Giardini (2005), Is a pyrolitic adiabatic mantle compatible with seismic data?, *Earth Planet. Sci. Lett.*, 232(3), 227–243, doi:10.1016/j.epsl.2005.01.031.

Cammarano, F., B. Romanowicz, L. Stixrude, C. Lithgow-Bertelloni, and W. Xu (2009), Inferring the thermochemical structure of the upper mantle from seismic data, *Geophys. J. Int.*, 179(2), 1169–1185, doi:10.1111/j.1365-246X.2009.04338.x.

Cao, A., and A. Levander (2010), High-resolution transition zone structures of the Gorda Slab beneath the western United States: Implication for deep water subduction, *J. Geophys. Res.*, 115, B07301, doi:10.1029/2009JB006876.

Christensen, U. R., and D. A. Yuen (1985), Layered convection induced by phase transitions, *J. Geophys. Res.*, 90(B12), 10,291–10,300, doi:10.1029/JB090iB12p10291.

Chudinovskikh, L., and R. Boehler (2004), $MgSiO_3$ phase boundaries measured in the laser-heated diamond cell, *Earth Planet. Sci. Lett.*, 219(3–4), 285–296, doi:10.1016/S0012-821X(04)00005-6.

Cobden, L., S. Goes, F. Cammarano, and J. Connolly (2008), Thermochemical interpretation of one-dimensional seismic reference models for the upper mantle: Evidence for bias due to heterogeneity, *Geophys. J. Int.*, 175(2), 627–648, doi:10.1111/j.1365-246X.2008.03903.x.

Cottaar, S., T. Heister, I. Rose, and C. Unterborn (2014), BurnMan: A lower mantle mineral physics toolkit, *Geochem. Geophys. Geosyst.*, 15, 1164–1179, doi:10.1002/2013GC005122.

Crotwell, H. P., T. J. Owens, and J. Ritsema (1999), The TauP Toolkit: Flexible seismic travel-time and ray-path utilities, *Seismol. Res. Lett.*, 70(2), 154–160, doi:10.1785/gssrl.70.2.154.

Day, E. A., and A. Deuss (2013), Reconciling PP and P′P′ precursor observations of a complex 660 km seismic discontinuity, *Geophys. J. Int.*, 194(2), 834–838, doi:10.1093/gji/ggt122.

Deuss, A., S. Redfern, K. Chambers, and J. Woodhouse (2006), The nature of the 660-kilometer discontinuity in Earth's mantle from global seismic observations of PP precursors, *Science*, 311, 198–201.

Dueker, K. G., and A. F. Sheehan (1997), Mantle discontinuity structure from midpoint stacks of converted *P* to *S* waves across the Yellowstone hotspot track, *J. Geophys. Res.*, 102(B4), 8313–8327, doi:10.1029/96JB03857.

Dziewonski, A. M., and D. L. Anderson (1981), Preliminary reference Earth model, *Phys. Earth Planet. Inter.*, 25(4), 297–356, doi:10.1016/0031-9201(81)90046-7.

Emry, E. L., A. A. Nyblade, J. Julià, S. Anandakrishnan, R. C. Aster, D. A. Wiens, A. D. Huerta, and T. J. Wilson (2015), The mantle transition zone beneath West Antarctica: Seismic evidence for hydration and thermal upwellings, *Geochem. Geophys. Geosyst.*, 16, 40–58, doi:10.1002/2014GC005588.

Faccenna, C., L. Jolivet, C. Piromallo, and A. Morelli (2003), Subduction and the depth of convection in the Mediterranean mantle, *J. Geophys. Res.*, 108(B2), 2099, doi:10.1029/2001JB001690.

Frost, D., and D. Dolejš (2007), Experimental determination of the effect of H_2O on the 410-km seismic discontinuity, *Earth Planet. Sci.Lett.*, 256(1–2), 182–195, doi:10.1016/j.epsl.2007.01.023.

Fukao, Y., and M. Obayashi (2013), Subducted slabs stagnant above, penetrating through, and trapped below the 660 km discontinuity, *J. Geophys. Res. Solid Earth*, 118, 5920–2938, doi:10.1002/2013JB010466.

Garel, F., S. Goes, D. R. Davies, J. H. Davies, S. C. Kramer, and C. R. Wilson (2014), Interaction of subducted slabs with the mantle transition-zone: A regime diagram from 2-D thermo-mechanical models with a mobile trench and an overriding plate, *Geochem. Geophys. Geosyst.*, 15, 1739–1765, doi:10.1002/2014GC005257.

Ghosh, S., E. Ohtani, K. D. Litasov, A. Suzuki, D. Dobson, and K. Funakoshi (2013), Effect of water in depleted mantle on post-spinel transition and implication for 660km seismic discontinuity, *Earth Planet. Sci. Lett.*, 371–372, 103–111, doi:10.1016/j.epsl.2013.04.011.

Hernández, E., J. Brodholt, and D. Alfè (2015), Structural, vibrational and thermodynamic properties of Mg_2SiO_4 and $MgSiO_3$ minerals from first-principles simulations, *Phys. Earth Planet. Inter.*, 240, 1–24, doi:10.1016/j.pepi.2014.10.007.

Hirose, K., T. Komabayashi, M. Murakami, and K.-i. Funakoshi (2001), In situ measurements of the majorite-akimotoite-perovskite phase transition boundaries in $MgSiO_3$, *Geophys. Res. Lett.*, 28(23), 4351–4354, doi:10.1029/2001GL013549.

Ito, E., and E. Takahashi (1989), Postspinel transformations in the system $Mg_2SiO_4 - Fe_2SiO_4$ and some geophysical implications, *J. Geophys. Res.*, 94, 10,637–10,646, doi:10.1029/JB094iB08p10637.

Jacobsen, S. D., and J. R. Smyth (2006), Effect of water on the sound velocities of ringwoodite in the transition zone, in *Earth's Deep Water Cycle, Geophys. Monogr. Ser.*, vol. 168, edited by S. D. Jacobsen and S. Van Der Lee, pp. 131–145, AGU, Washington, D. C., doi:10.1029/168GM10.

Jenkins, J., S. Cottaar, R. S. White, and A. Deuss (2016), Depressed mantle discontinuities beneath Iceland: Evidence of a garnet controlled 660 km discontinuity?, *Earth Planet. Sci. Lett.*, *433*, 159–168, doi:10.1016/j.epsl.2015.10.053.

Katsura, T., and E. Ito (1989), The system $Mg_2SiO_4 - Fe_2SiO_4$ at high pressures and temperatures: Precise determination of stabilities of olivine, modified spinel, and spinel, *J. Geophys. Res.*, *94*, 15,663–15,670.

Katsura, T., et al. (2004), Olivine-wadsleyite transition in the system $(Mg, Fe)_2SiO_4$, *J. Geophys. Res.*, *109*, B02209, doi:10.1029/2003JB002438.

King, S. D., D. J. Frost, and D. C. Rubie (2015), Why cold slabs stagnate in the transition zone, *Geology*, *43*(3), 231–234, doi:10.1130/G36320.1.

Knapmeyer-Endrun, B., F. Krüger, C. Legendre, and W. Geissler (2013), Tracing the influence of the Trans-European Suture Zone into the mantle transition zone, *Earth Planet. Sci. Lett.*, *363*, 73–87, doi:10.1016/j.epsl.2012.12.028.

Langston, C. A. (1977), Corvallis, Oregon, crustal and upper mantle receiver structure from teleseismic *P* and *S* waves, *Bull. Seismol. Soc. Am.*, *67*(3), 713–724.

Lawrence, J. F., and P. M. Shearer (2006), A global study of transition zone thickness using receiver functions, *J. Geophys. Res.*, *111*, B06307, doi:10.1029/2005JB003973.

Lebedev, S., S. Chevrot, and R. van der Hilst (2003), Correlation between the shear-speed structure and thickness of the mantle transition zone, *Phys. Earth Planet. Inter.*, *136*(1–2), 25–40, doi:10.1016/S0031-9201(03)00020-7.

Lee, S.-H., J. Rhie, Y. Park, and K.-H. Kim (2014), Topography of the 410 and 660 km discontinuities beneath the Korean Peninsula and southwestern Japan using teleseismic receiver functions, *J. Geophys. Res. Solid Earth*, *119*, 7245–7257, doi:10.1002/2014JB011149.

Lekic, V., S. W. French, and K. M. Fischer (2011), Lithospheric thinning beneath rifted regions of Southern California, *Science*, *334*(6057), 783–787, doi:10.1126/science.1208898.

Ligorria, J. P., and C. J. Ammon (1999), Iterative deconvolution and receiver-function estimation, *Bull. Seismol. Soc. Am.*, *89*(5), 1395–1400.

Litasov, K., E. Ohtani, A. Sano, A. Suzuki, and K. Funakoshi (2005a), In situ X-ray diffraction study of post-spinel transformation in a peridotite mantle: Implication for the 660-km discontinuity, *Earth Planet. Sci. Lett.*, *238*(3–4), 311–328, doi:10.1016/j.epsl.2005.08.001.

Litasov, K. D., E. Ohtani, A. Sano, A. Suzuki, and K. Funakoshi (2005b), Wet subduction versus cold subduction, *Geophys. Res. Lett.*, *32*, L13312, doi:10.1029/2005GL022921.

Lombardi, D., J. Braunmiller, E. Kissling, and D. Giardini (2009), Alpine mantle transition zone imaged by receiver functions, *Earth Planet. Sci. Lett.*, *278*(3–4), 163–174, doi:10.1016/j.epsl.2008.11.029.

Mohamed, A. A., S. S. Gao, A. A. Elsheikh, K. H. Liu, Y. Yu, and R. E. Fat-Helbary (2014), Seismic imaging of mantle transition zone discontinuities beneath the northern Red Sea and adjacent areas, *Geophys. J. Int.*, *199*(2), 648–657, doi:10.1093/gji/ggu284.

Molinari, I., and A. Morelli (2011), EPcrust: A reference crustal model for the European Plate, *Geophys. J. Int.*, *185*(1), 352–364, doi:10.1111/j.1365-246X.2011.04940.x.

Morais, I., L. Vinnik, G. Silveira, S. Kiselev, and L. Matias (2015), Mantle beneath the Gibraltar Arc from receiver functions, *Geophys. J. Int.*, *200*(2), 1153–1169, doi:10.1093/gji/ggu456.

Nolet, G., and F. A. Dahlen (2000), Wave front healing and the evolution of seismic delay times, *J. Geophys. Res.*, *105*(B8), 19,043–19,054, doi:10.1029/2000JB900161.

Ohtani, E. (2015), Hydrous minerals and the storage of water in the deep mantle, *Chem. Geol.*, *418*, 6–15, doi:10.1016/j.chemgeo.2015.05.005.

Ozacar, A., H. Gilbert, and G. Zandt (2008), Upper mantle discontinuity structure beneath East Anatolian Plateau (Turkey) from receiver functions, *Earth Planet. Sci. Lett.*, *269*(3–4), 427–435, doi:10.1016/j.epsl.2008.02.036.

Panero, W. R. (2010), First principles determination of the structure and elasticity of hydrous ringwoodite, *J. Geophys. Res.*, *115*, B03203, doi:10.1029/2008JB006282.

Pearson, D. G., et al. (2014), Hydrous mantle transition zone indicated by ringwoodite included within diamond, *Nature*, *507*(7491), 221–224, doi:10.1038/nature13080.

Ringwood, A. (1970), Phase transformations and the constitution of the mantle, *Phys. Earth Planet. Inter.*, *3*, 109–155, doi:10.1016/0031-9201(70)90047-6.

Schmandt, B., K. Dueker, E. Humphreys, and S. Hansen (2012), Hot mantle upwelling across the 660 beneath Yellowstone, *Earth Planet. Sci. Lett.*, *331–332*, 224–236, doi:10.1016/j.epsl.2012.03.025.

Simmons, N., and H. Gurrola (2000), Multiple seismic discontinuities near the base of the transition zone in the Earth's mantle, *Nature*, *405*, 559–562, doi:10.1038/35014589.

Stixrude, L., and C. Lithgow-Bertelloni (2011), Thermodynamics of mantle minerals - II. Phase equilibria, *Geophys. J. Int.*, *184*(3), 1180–1213.

Suetsugu, D., et al. (2010), Depths of the 410-km and 660-km discontinuities in and around the stagnant slab beneath the Philippine Sea: Is water stored in the stagnant slab?, *Phys. Earth Planet. Inter.*, *183*(1–2), 270–279, doi:10.1016/j.pepi.2010.09.004.

Tarits, P., S. Hautot, and F. Perrier (2004), Water in the mantle: Results from electrical conductivity beneath the French Alps, *Geophys. Res. Lett.*, *31*, L06612, doi:10.1029/2003GL019277.

Tauzin, B., and Y. Ricard (2014), Seismically deduced thermodynamics phase diagrams for the mantle transition zone, *Earth Planet. Sci. Lett.*, *401*, 337–346, doi:10.1016/j.epsl.2014.05.039.

Tauzin, B., R. D. van der Hilst, G. Wittlinger, and Y. Ricard (2013), Multiple transition zone seismic discontinuities and low velocity layers below western United States, *J. Geophys. Res. Solid Earth*, *118*, 2307–2322, doi:10.1002/jgrb.50182.

Thompson, D. A., J. O. S. Hammond, J.-M. Kendall, G. W. Stuart, G. R. Helffrich, D. Keir, A. Ayele, and B. Goitom (2015), Hydrous upwelling across the mantle transition zone beneath the Afar Triple Junction, *Geochem. Geophys. Geosyst.*, *16*, 834–846, doi:10.1002/2014GC005648.

Utada, H., T. Koyama, M. Obayashi, and Y. Fukao (2009), A joint interpretation of electromagnetic and seismic tomography models suggests the mantle transition zone below Europe is dry, *Earth Planet. Sci. Lett.*, *281*(3–4), 249–257, doi:10.1016/j.epsl.2009.02.027.

van der Lee, S., and D. A. Wiens (2006), Seismological constraints on Earth's deep water cycle, in *Earth's Deep Water Cycle, Geophys. Monogr. Ser.*, vol. 168, edited by S. D. Jacobsen and S. Van Der Lee, pp. 13–27, AGU, Washington, D. C.

van der Meijde, M., S. van der Lee, and D. Giardini (2005), Seismic discontinuities in the Mediterranean mantle, *Phys. Earth Planet. Inter.*, *148*(2–4), 233–250, doi:10.1016/j.pepi.2004.09.008.

Vinnik, L. (1977), Detection of waves converted from *P* to SV in the mantle, *Phys. Earth Planet. Inter.*, *15*(1), 39–45, doi:10.1016/0031-9201(77)90008-5.

Wentzcovitch, R., B. Karki, M. Cococcioni, and S. de Gironcoli (2004), Thermoelastic properties of $MgSiO_3$-perovskite: Insights on the nature of the Earth's lower mantle, *Phys. Rev. Lett.*, *92*(1), 018501, doi:10.1103/PhysRevLett.92.018501.

Wortel, M. J. R., and W. Spakman (2000), Subduction and slab detachment in the Mediterranean-Carpathian Region, *Science*, *290*(5498), 1910–1917, doi:10.1126/science.290.5498.1910.

Xu, W., C. Lithgow-Bertelloni, L. Stixrude, and J. Ritsema (2008), The effect of bulk composition and temperature on mantle seismic structure, *Earth Planet. Sci. Lett.*, *275*(1–2), 70–79, doi:10.1111/j.1365-246X.2010.04890.x.

Ye, Y., C. Gu, S.-H. Shim, Y. Meng, and V. Prakapenka (2014), The postspinel boundary in pyrolitic compositions determined in the laser-heated diamond anvil cell, *Geophys. Res. Lett.*, *41*, 3833–3841, doi:10.1002/2014GL060060.

Yu, Y. G., R. M. Wentzcovitch, T. Tsuchiya, K. Umemoto, and D. J. Weidner (2007), First principles investigation of the postspinel transition in Mg_2SiO_4, *Geophys. Res. Lett.*, *34*, L10306, doi:10.1029/2007GL029462.

Yu, Y. G., R. M. Wentzcovitch, V. L. Vinograd, and R. J. Angel (2011), Thermodynamic properties of $MgSiO_3$ majorite and phase transitions near 660 km depth in $MgSiO_3$ and Mg_2SiO_4: A first principles study, *J. Geophys. Res.*, *116*, B02208, doi:10.1029/2010JB007912.

Zhu, H., E. Bozdağ, D. Peter, and J. Tromp (2012), Structure of the European upper mantle revealed by adjoint tomography, *Nat. Geosci.*, *5*(7), 493–498, doi:10.1038/ngeo1501.

Zhu, H., E. Bozdağ, T. S. Duffy, and J. Tromp (2013), Seismic attenuation beneath Europe and the North Atlantic: Implications for water in the mantle, *Earth Planet. Sci. Lett.*, *381*, 1–11, doi:10.1016/j.epsl.2013.08.030.

Zhu, H., E. Bozdağ, and J. Tromp (2015), Seismic structure of the European upper mantle based on adjoint tomography, *Geophys. J. Int.*, *201*(1), 18–52, doi:10.1093/gji/ggu492.